

Kinetic simulation of magnetic field generation and collisionless shock formation in expanding laboratory plasmas

W. Fox,^{1,2,*} J. Matteucci,² C. Moissard,³ D. B. Schaeffer,² A. Bhattacharjee,^{1,2} K. Germaschewski,⁴ and S.X. Hu⁵

¹*Princeton Plasma Physics Laboratory, Princeton, NJ 08543, USA*

²*Department of Astrophysical Sciences, Princeton University, Princeton, NJ 08544, USA*

³*Laboratoire de Physique des Plasmas, École Polytechnique, Paris 75252, France*

⁴*Space Science Center, University of New Hampshire, Durham, New Hampshire 03824, USA*

⁵*Laboratory for Laser Energetics, University of Rochester, Rochester, New York 14623, USA*

Recent laboratory experiments with laser-produced plasmas have observed and studied a number of fundamental physical processes relevant to magnetized astrophysical plasmas, including magnetic reconnection, collisionless shocks, and magnetic field generation by Weibel instability, opening up new experimental platforms for laboratory astrophysics. We develop a fully kinetic simulation model for first-principles simulation of these systems including the dynamics of magnetic fields—magnetic field generation by the Biermann battery effect or Weibel instability; advection by the ion flow, Hall effect, and Nernst effect; and destruction of the field by dissipative mechanisms. Key dimensionless parameters describing the system are derived for scaling between kinetic simulation, recent experiments, and astrophysical plasmas. First, simulations are presented which model Biermann battery magnetic field generation in plasmas expanding from a thin target. Ablation of two neighboring plumes leads to the formation of a current sheet as the opposing Biermann-generated fields collide, modeling recent laser-driven magnetic reconnection experiments. Second, we simulate recent experiments on collisionless magnetized shock generation, by expanding a piston plasma into a pre-magnetized ambient plasma. For parameters considered, the Biermann effect generates additional magnetic fields in the curved shock front and thereby increases shock particle reflection. Both cases show the importance of kinetic processes in the interaction of plasmas with magnetic fields, and open opportunities to benchmark these important processes through comparison of theory and experiments.

I. INTRODUCTION

Laboratory experiments provide valuable platforms to test fundamental physics behind astrophysical plasmas. Studying and comparing the common physical processes between systems with such differing varying spatial and temporal scales is possible because of universality of the processes, embodied in scaling similarity of the underlying equations [1, 2]. The recent generation of laser facilities allows observation and study of a variety of processes in magnetized plasmas relevant to plasma astrophysics. Expanding laser-produced plasmas readily produce fast supersonic flows, and the plasmas can be magnetized either through self-magnetization, or can be expanded into plasmas pre-magnetized with an externally applied field. Recent laser facilities couple sufficient energy into the plasma to obtain high-temperature, collisionless regimes while simultaneously being large enough for scale separation between global scales and kinetic scales. The subsequent dynamics of the magnetized plasmas are of fundamental interest and have broad relevance to some of the most energetic processes in astrophysical plasmas, including shock formation, magnetic reconnection, kinetic instabilities, and particle energization.

Strong, MG-scale magnetic fields can be generated in expanding laser plasmas by the Biermann battery effect

[e.g. 3–6], or by kinetic instabilities such as Weibel instability [7, 8] and Rayleigh-Taylor instability [9, 10]. These processes all have astrophysical analogues, allowing experimental investigation of the generation of magnetic fields and subsequent dynamics of magnetized plasmas in scaled laboratory astrophysics experiments. The Biermann battery effect has been proposed to provide primordial, seed magnetic fields in the cosmos, which can then be subsequently amplified by turbulence [11]. The ion-Weibel instability is important for generating a turbulent magnetic field in interpenetrating plasmas, mediating collisionless astrophysical shocks in unmagnetized or weakly magnetized regimes [12, 13]. The interaction of magnetized flows can also steepen into magnetized shocks [14, 15]. Collision of magnetized plasmas can drive magnetic reconnection, which is an important mechanism for converting magnetic energy back to particle flows, heat, and energized particles [16–18]. The development of both reconnection and shock experiments on laser facilities will potentially allow comparison of the efficiency of these two processes for energizing particles in astrophysics.

The evolution of the magnetic field in a plasma is determined from the Generalized Ohm’s law, via Faraday’s law. In laser-produced plasmas, the Ohm’s law can be written as [19]:

$$\mathbf{E} = \eta \mathbf{j} - \mathbf{v} \times \mathbf{B} + \frac{\mathbf{j} \times \mathbf{B}}{ne} - \mathbf{v}_T \times \mathbf{B} - \frac{\nabla p_e}{ne} - \frac{\nabla \cdot \mathbf{\Pi}_e}{ne}. \quad (1)$$

The terms on the RHS enumerate the effects which evolve the field at scales ranging from global to kinetic scales,

* wfox@pppl.gov

which include resistive dissipation ($\eta\mathbf{j}$); advection of the magnetic field by the bulk fluid ($\mathbf{v} \times \mathbf{B}$), the Hall effect ($\mathbf{j} \times \mathbf{B}$), and the Nernst effect ($\mathbf{v}_T \times \mathbf{B}$), where \mathbf{v}_T is proportional to the heat flux; the pressure term (∇p_e), which allows electrothermal magnetic field generation; and momentum transport embodied in the pressure tensor ($\nabla \cdot \mathbf{\Pi}_e$). The electron pressure can lead to magnetic field generation in regions where the temperature and density gradients are not collinear (leading to finite $\nabla \times \mathbf{E}$), in what is often called the Biermann battery effect [11]. The Nernst effect [20], which is advection of magnetic field by the heat flux, can be important in semi-collisional regimes and results from the v^{-3} dependence of the Coulomb collision frequency; intuitively, it can be understood from the idea that the magnetic field remains frozen to a population of “hot” electrons but is allowed to diffuse across the cold compensating return current. Finally, momentum transport, i.e. off-diagonal pressure tensor ($\nabla \cdot \mathbf{\Pi}$), is often important for breaking magnetic field lines in magnetic reconnection current sheets in collisionless regimes [21].

Modeling the dynamics of energy exchange between the magnetic field, plasma flows, and energized particles in these systems is a computational grand challenge, because the relevant processes (magnetic reconnection and shocks) couple global scales with plasma kinetic scales (the ion and electron skin depths) characteristic of reconnection current sheets or shock ramps, yielding a challenging, multi-scale kinetic plasma problem. Fully kinetic simulations are important tools for intrinsically kinetic processes, especially for Weibel instability and for collisionless shocks, where particle distributions develop strong counter-streaming components significantly deviant from a thermal description. As another example, during magnetic reconnection in collisionless and weakly-collisional regimes, the field-line breaking is typically mediated by momentum transport, a kinetic effect resulting from meandering electron orbits in the current sheet. A final example is in strongly-driven, semi-collisional regimes, where the heat flux can advect the magnetic fields via the Nernst effect [20, 22, 23]. Challenges remain to correctly model the Nernst effect when the heat-flux becomes non-local and deviates from classical predictions. While interesting ongoing progress has aimed to identify closures for including all these processes within fluid simulations, including for magnetic reconnection [24, 25] and Biermann battery field generation proximate to shocks [26], for the foreseeable future fully kinetic particle simulations will play a vital role in simulating these processes.

Particle-in-cell (PIC) methods solve the kinetic Vlasov-Maxwell system using quasi-particles to represent particle phase space. The quasi-particles evolve according to the equations of motion for the particles, interacting with the electromagnetic fields on a mesh; the fields in turn evolve according to Maxwell’s equations, with current sources determined self-consistently by the particles. While highly computationally intensive, modern imple-

mentations of the PIC technique scale well to the largest supercomputers. Here we use the PSC code [27] and develop techniques to simulate large volumes of laser-plasma with PIC simulation. We note that particle simulations have long been used for high-intensity relativistic short-pulse (ps- and fs-class) laser-plasma interaction [e.g. 28]; here we present how these techniques are generalized to study much larger volumes (presently cm^2 in 2-D or mm^3 in 3-D) and longer time scales (ns), where it is not practical to resolve the laser wavelength.

In this paper we develop a fully kinetic ablation model for first-principles and end-to-end simulation of recent laser-plasma experiments on magnetic reconnection [29–33], Weibel instability [7, 8] and collisionless magnetized shocks [34, 35]. In the first part of the paper, we simulate Biermann battery magnetic field generation and evolution from spatially localized heating in a thin target. This enables simulation of multiple colliding plumes, in which the plume collision compresses the opposing Biermann fields into a current sheet drives magnetic reconnection [29–31, 33]. Previous simulations of reconnection in these plasmas have largely relied on simplified models and geometries [36–38], and, while many physics insights into reconnection in these systems have come from these simulations, they are also limited for comparison with experiment because they require many initial parameters to be put in by hand. The model we describe here allows end-to-end simulation of these experiments, and we present simulations of the 2-D evolution of colliding plumes up through the time of current sheet formation. Capturing the field generation and plume expansion has significant physical implications, as the plasma parameters which determine the magnetic reconnection regime (such as density in the reconnection layer, velocity driving the inflow, and local magnetic fields) are ultimately determined by the evolution of the plasmas up through the current sheet formation process. It also enables full 3-D simulations of magnetic reconnection in these systems, which will be reported separately [39].

In the second half of this paper, we simulate the evolution of ablated plasma into a pre-existing, magnetized background plasma, as has been studied in recent experiments on strongly-driven magnetic reconnection [32], and formation of collisionless magnetized shocks [35]. The development of this platform will allow for a number of studies in high-Mach number shocks ($M \gtrsim 5$) including particle acceleration and particle heating by shocks, and shock dynamics including reformation and instabilities. The simulations played an important role in the development of this experimental platform by showing how the system behaves for a range of driving parameters, building intuition about the physics of the available experimental regimes. In the case of magnetized shocks, the simulations also predicted observables such as the development of “double density jumps” in the collisionless shock front. Here we present the details of this simulation model, and present large-scale 2-D simulations which show physics associated with the higher-dimensionality

expanding shocks, including Biermann battery magnetic field within the shock front. For the parameters considered quantitatively modifies the shock by increasing particle reflection. Weibel instability is also observed upstream and downstream of the shock [40] consistent with instability of the counterstreaming ion populations generated by these high-Mach number shocks.

II. SIMULATION MODEL

Fully kinetic PIC simulations are conducted to model the plasma evolution and magnetic field generation in plasma rapidly expanding from a thin, high-density target, enabling direct kinetic modeling of recent laser-plasma experiments. The key point of the model is to match heating and plasma conditions to separate, off-line radiation hydrodynamic (RH) simulations using the DRACO code [41], providing rigorous and well-benchmarked parameters from which to drive the kinetic simulations. The scheme of matching the relevant dimensionless parameters from the simulation model to experiments is discussed below. For experimental fidelity, the model includes particle collisions which allows collisional effects such as magnetic field diffusion due to resistivity and magnetic field advection by the Nernst effect. Particle simulations are conducted using the PSC code [27], which can run on recent leadership scale computing facilities with good scaling and includes GPU support.

The kinetic ablation model applies a volumetric heating operator to a thin target to heat the target and drive an expanding ablation plume. The target region is simultaneously kept at constant density n_s by continually adding particles, mimicking the infinite reservoir provided by a solid density target. The heated region expands as an ablation flow into the neighboring low density plasma or vacuum. In our model, the sonic point occurs at $n_{ab} = 0.4 n_s$; therefore our model includes plasma density up to about 2.5 times the critical density. The plumes are observed to obtain a quasi-isothermal electron temperature T_{ab} , which depends on the magnitude of the heating. In the simulation, we adjust the heating to provide a desired T_{ab} .

Off-line DRACO RH simulations using reported laser parameters provide input to drive the kinetic PSC simulations, by the following procedure. First, the DRACO simulations are conducted and analyzed. These simulations generate an expanding plasma plume profile in which a characteristic “knee” forms in the density at the sonic point of the ablative plasma flow. This ablation point defines the ablation density n_{ab} which is matched to the PIC model. Secondly, outside the knee, the plasma is typically nearly isothermal, and this provides an ablation temperature T_{ab} . These provide the dimensional parameters for driving a scaled PSC simulation. We find that by matching n_{ab} and T_{ab} in PSC, the remaining hydro-dynamic evolution outside the ablation point is reasonably well-matched between the two simulations.

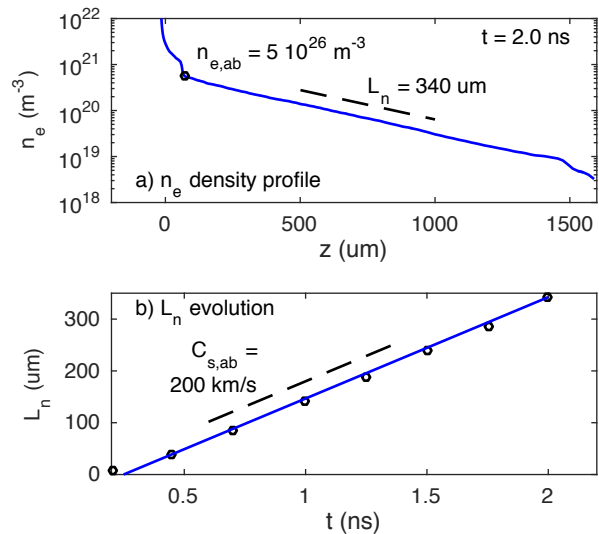


FIG. 1. Expanding plasma evolution predicted by DRACO, demonstrating measurement of parameters to drive PSC simulations. (a) n_e profile off the target, showing identification of n_{ab} and the density scale length L_n (b) Evolution of the scale length. In this DRACO simulation, the density evolution $\langle L_n \rangle$ agrees quantitatively with the ablation sound speed $C_{s,ab} \approx 2.0 \times 10^5$ m/s.

We note again PSC does not independently predict n_{ab} and T_{ab} because it does not have a laser ray-trace energy-deposition model; this is the driving input from DRACO simulations. Secondly, the PSC simulations do not include many features of the RH simulations, such as acceleration of the solid target by ablation pressure and outward motion of the ablation surface.

A. Dimensionless parameters

Despite operating at vastly different length and time scales, results from laboratory experiments can be applied to understanding astrophysical phenomena, through scaling laws. This is furnished by the nature of the underlying equations, where it can be shown that systems are *similar* such that the results can be scaled between systems, provided that the relevant dimensionless parameters are matched [1]. The same set of considerations is necessary for numerical simulations as well, as the latter are often conducted in dimensionless unit systems. What is interesting is these considerations can allow new simulation techniques to be applied, such as explicit PIC simulations as developed here, by serving as a navigational aid in determining which parameters are most important to match, and which need only be matched “in regime”. This is important because explicit PIC is a powerful technique, but also cannot match every dimensionless parameter, especially those involving the separation of electron and ion scales, due to compu-

tational cost.

To begin with, it is useful to determine the “ion-scale” parameters for this family of systems. We do this, assume that the plasma dynamics depends on the following parameters: a characteristic density and temperature n_0 and T_0 , the ion mass M_i , ion charge Ze , μ_0 , and a spatial scale R , for example the heating radius. Then by Buckingham’s Pi theorem [2], given the 4 dimensional quantities (length, time, mass, charge), these 6 dimensional parameters collapse to a much smaller space of only 2 dimensionless parameters: R/d_{i0} and nd_{i0}^3 . The first parameter defines the scale separation between the global scale and ion-kinetic scale and is fundamental for this whole class of problems. The second parameter nd_{i0}^3 is usually much larger than unity and is related to the particle discreteness and collisionality, and will return as a collisionality parameter in the discussion below. The collisionality can be related to both the plasma viscosity and magnetic diffusivity, as is commonly considered in scaling analysis of the MHD equations for laboratory astrophysics [1].

As discussed above, n_{ab} and T_{ab} are two important parameters describing the coronal plasma. These two parameters form the basis for scaling the length and time scales of the coronal plasma via the “ion-scale” parameters. We define the ion skin depth $d_{i0} = (M_i/n_{ab}Ze^2\mu_0)^{1/2}$ based on n_{ab} and the characteristic ion species. This provides the fundamental length unit of the simulations. Second, we define the ablation sound speed, $C_{s,ab} = (ZT_{ab}/M_i)^{1/2}$. Together these define a characteristic ablation timescale $t_d = d_{i0}/C_{s,ab}$. The scaling behavior enforces that the solutions for the various physical quantities can be written as a function of the dimensionless parameters and scaled coordinates, e.g. for the density, $n = n_{ab}f(x/d_{i0}, t/t_d)$. The classical 1-D “ablation flow” solution [42], $n = n_{ab} \exp[-(x/C_s t)]$ exactly accords with this scaling behavior, since $C_s = d_{i0}/t_d$.

The parameters also define a fundamental magnetic field scale $B_0 = (\mu_0 n_{ab} T_{ab})^{1/2}$. Conveniently, in these units, $t\omega_{ci} = (B/B_0)(t/t_d)$, and the local plasma $\beta = 0.5(n/n_{ab})(T/T_{ab})(B/B_0)^{-2}$. The fundamental unit of magnetic vector potential, $A_0 = d_{i0}B_0 = (1/e)(T_{ab}M_i/Ze)^{1/2}$, is the integrated field (flux) sufficient to force ions at the sound speed to gyrate. In the case with pre-applied magnetic fields, the upstream magnetic field is parameterized by a further dimensionless parameter B_{up}/B_0 . The fundamental electric field is $E_0 = C_s B_0 = T_{ab}/d_{i0}$. These scales are used below to convert simulation results to physical units.

Explicit PIC simulations require two additional electron-scale parameters, Zm_e/M_i , the electron-ion mass ratio, and $T_{ab}/m_e c^2$, which describes the speed of light in the system. These parameters describe the scale separation of electron-ion physics and electrostatic phenomena, as $d_e/d_i = (Zm_e/M_i)^{1/2}$, and $\lambda_D/d_{e0} = (T_{ab}/m_e c^2)^{1/2}$, where λ_D is the Debye length. A common technique in explicit PIC simulations (of magnetic reconnection and shocks) is to compress these parameters com-

pared to their physical values so that they are matched in regime rather than exactly [e.g. 13, 21, 36, 40, 43]. This allows important physical insights to be obtained from fully kinetic simulation within reasonable computational cost, and tests can be conducted to verify the convergence of the simulation results with respect to the reduced parameters.

Finally, collisional processes in the plasma may be important to include for experimental fidelity, by allowing thermalization of the distribution functions, or dissipation processes such as magnetic field diffusion. In PSC, Coulomb collisions are modeled using the Takizuka-Abe binary collision model [27], which is essentially equivalent to the Landau collision operator. This introduces an additional time-scale, the electron-ion collision time $\tau_{ei} = \nu_{ei}^{-1}$. In the PSC code, ν_{ei} is a free parameter; therefore, it generates an additional dimensionless parameter to match to the physical system. We match the collisionality via the dimensionless parameter $\nu_{ei0}/\omega_{ce0} = d_{e0}/\lambda_{mfp0}$, as this determines the magnetization character for electrons in the Braginskii transport. Here ν_{ei0} and $\lambda_{mfp0} = \sqrt{T_{ab}/m_e}/\nu_{ei0}$ are the electron collision frequency and mean-free path evaluated at n_{ab} and T_{ab} , and ω_{ce0} is the electron gyro-frequency at $B = B_0$. Matching this dimensionless parameter also obtains the correct collisional diffusivity of the magnetic field. To show this, we calculate a magnetic Reynold’s number based on sonic flows, $R_M \equiv \mu_0 L C_s / \eta$, where L is the system size and η the collisional resistivity. With a small amount of algebra, $R_M = (L/d_i) \cdot (\lambda_{mfp0}/d_{e0})$, which indicates that matching L/d_{i0} as an ion-scale parameter, and matching electron collisionality according to λ_{mfp0}/d_{e0} , obtains the correct magnetic Reynold’s number. We do note that, following this scheme, the electron collisionality connected to global time or length scales, L/λ_{mfp0} , or $\nu_{ei0}t_d$ are only matched quantitatively if the physical mass ratio is also matched. This impacts, for example, studies of non-local transport, where the electron mass dependence of the results would need to be carefully checked.

To summarize, in the kinetic ablation model, dimensional analysis has reduced the problem to a small number of dimensionless parameters: R/d_{i0} reflecting the scale separation between the global and ion-kinetic scale; λ_{mfp0}/d_{e0} reflecting the collisionality; and the electron-scale dimensionless parameters Zm_e/M_i and $m_e c^2/T_{ab}$. Additional applied magnetic fields are parameterized through $B_{up}/B_0 = B_{up}/(\mu_0 n_{ab} T_{ab})^{1/2}$.

B. Particle deposition and heating

As discussed above, kinetic ablation simulations maintain a high-density thin target region, which is topped up to mimic the reservoir of plasma provided by a solid-density target. During the simulation, particles are

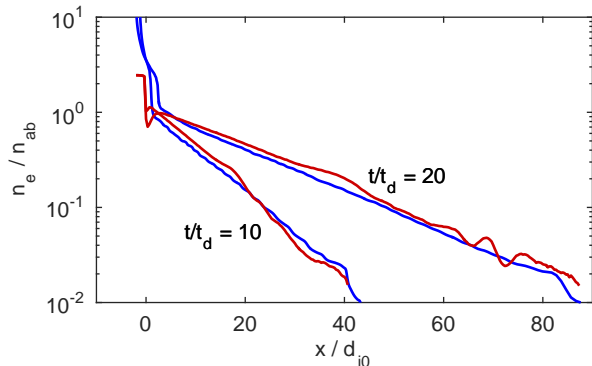


FIG. 2. Comparison of density profiles from DRACO (blue) and PSC (red), at two times.

topped up in the target region using an implicit method

$$n \rightarrow n + \frac{n_s - n}{1 + \tau_p / \Delta t_p} \quad \text{if } n < n_s, \quad (2)$$

where τ_p is a characteristic time to refill particles, and Δt_p is the time between calls to the particle deposition code. For a wide range of $\tau_p / \Delta t_p$ the density is kept close to n_s . Particles are added at a specified cold target temperature in appropriate electron-ion ratios to maintain a charge-neutral plasma.

Meanwhile, electrons are heated in the target by random kicks to the momentum vectors,

$$p_i \rightarrow p_i + (m_e H \Delta t_h)^{1/2} r \quad (3)$$

where r is a gaussian random variable with unity variance, Δt_h is the time between calls to the heating routine, and $H(x, y, z)$ is a spatially-dependent heating rate (eV/s). Δt_h reflects sub-cycling of the heating operator compared to the particle push timestep, for efficiency. The magnitude of H is adjusted to obtain a desired T_{ab} . A spatial profile can be applied to H , for example gaussian and super-gaussian shapes characteristic of laser foci, for localized heating and Biermann-battery field generation.

Despite its simplicity we find this model gives a good agreement for coronal plasma evolution compared to radiation-hydro simulation and analytic theory. Figure 2 shows a comparison of the plasma density between PSC and DRACO at two scaled times, showing the agreement. (For parameters, see Section IV.)

C. Further numerical details

The plasma evolves from a thin high-density target held at density n_s by the top-up method described above, with typical thickness $3d_{i0}$. Plasma expands into a background plasma at density $n_{bg} \ll n_{ab}$. For some systems, such as for the shock studies, the background density is an important parameter to match to experiment. The

background plasma and target are also initialized at a cold plasma temperature T_c . In physical experiments T_c is room temperature; here we simply require $T_c \ll T_{ab}$.

PSC simulations are conducted on a uniform grid with grid spacing Δx and Δz . We find that there are restrictions on the magnitude of Δx and Δz , so that Debye-scale numerical heating does not play a role on the time scale of the simulation. The most stringent location for numerical instability is in the initially cold high-density region. There the instability criterion is based on the Debye length calculated with T_c and n_s , and we find that for the PSC second-order particle shape, $\Delta x / \lambda_{D,c} < 50$ is required to avoid significant numerical heating on the simulation time scale, where $\lambda_{D,c} / d_{e0} = (n_{ab} / n_s)^{1/2} (T_c / m_e c^2)^{1/2}$

Finally, PSC simulations use macro-particles which represent a certain volume of phase space, and we typically find that 50 particles per cell representing n_s is sufficient to well-resolve the physics under study, though we typically use 200 or more in the 2-D simulations presented here.

III. MAGNETIC FIELD GENERATION AND EVOLUTION IN LASER-DRIVEN RECONNECTION EXPERIMENTS

The Biermann battery effect is important for magnetic field generation in both laser experiments and astrophysics. Non-collinear gradients of density and temperature lead to volumes with net circulating EMF which can drive currents and generate a magnetic field. The Biermann battery has also been proposed as a mechanism in astrophysics to generate primordial magnetic fields, predominantly near shocks, where the strong localized entropy production produces the sharp gradients for a strong thermoelectric effect [11]. In laser-plasma interaction, the effect is to self-magnetize the plasma, with a toroidal magnetic field wrapping around the laser focus. This was been observed and studied in a number of early experiments [3–5], with recent resurgence driven by new measurement techniques based on proton radiography [6, 44, 45], and use of multiple plasmas to drive magnetic reconnection between neighboring plumes at a small separation [29, 30, 33].

The experiments use pairs of laser-produced plumes from a flat target. The Biermann effect generates a strong magnetic field of order megagauss (MG), which forms a toroidal ribbon wrapping around the bubble. If multiple bubbles are created at small separation, the bubbles expand into one another, squeezing the opposing magnetic fields together and driving reconnection. Laser-driven magnetic reconnection experiments have the possibility to significantly advance understanding of laboratory reconnection by, first, obtaining data on the reconnection behavior of large systems (measured by the ratio of the system size to fundamental plasma scales such as the ion inertial length d_i). To date, the majority of ded-

icated laboratory experiments [18] have been conducted at moderate system sizes, where two-fluid effects have been demonstrated to be important for obtaining fast reconnection [46]. In large systems it is proposed that the tearing or plasmoid instability can break the current into a hierarchy of meso-scale current sheets undergoing fast reconnection. Second, these experiments can measure the efficiency of particle acceleration by reconnection, again in large systems. Significant particle energization is inferred to occur in many astrophysical environments, and magnetic reconnection has been proposed to be the driver in many cases, including the Earth's magnetotail [16, 47], solar flares [48], the Crab nebula and pulsar [49], and extragalactic jets [50].

Previous simulations have considered the reconnection in parameter regimes of HEDP plasmas, and with model geometries of colliding bubbles to assess reconnection mechanisms and particle acceleration. Simulations have demonstrated the role of flux pile-up [36], the breakup of the current sheet into multiple islands at large system size [37], and have documented mechanisms for generating electron jets and accelerating particles [38, 43, 51, 52]. Recent kinetic simulations have also studied Biermann-battery magnetic field generation in collisionless plasmas with model initial conditions [53].

Here we present a kinetic simulation of the full development of the current sheet between colliding plasmas, including the initial Biermann-battery field generation, advection and collision of the fields, which thin down and compress into a current sheet where the magnetic fields reverse over a narrow region. Through analysis of the Ohm's law we quantitatively assess the various roles of the Biermann effect for generating field and subsequent advection by the plasma flow, Hall effect, and Nernst effect. The results show a supersonic advection of the magnetic field by the Hall effect which has not been previously identified. This work forms the basis for comparison of field generation and advection with detailed experiments and complementary simulation techniques such as radiation-hydrodynamics which includes magnetic field effects [45, 54]. Full 3-D simulations which include reconnection will be presented in a followup paper.

We first briefly review the Biermann battery magnetic field generation mechanism. To understand the mechanism of B-field generation, we first re-write the Ohm's law, keeping the plasma currents to make the causation more transparent, and ignoring collisions for the time being

$$(m_e/n_e e^2) \frac{d}{dt} \mathbf{j} = \nabla p_e/n_e + \mathbf{E}. \quad (4)$$

Now, consider a volume in the plasma with finite $\nabla p_e/n_e$, with ∇p_e non-parallel to ∇n , and consider a loop in the plane defined by the vectors $\nabla n \times \nabla T$. If these two vectors are not everywhere parallel, then n is not a function of T , and integration of $\nabla p_e/n_e$ around the loop is in general non-zero; indeed by Stoke's theorem, $\oint (\nabla p_e/n_e) \cdot ds = \int (1/n_e) (\nabla n_e \times \nabla T_e) \cdot d\mathbf{A}$, for a

given path ds following the boundary of the surface $d\mathbf{A}$. This "battery" produces a net electromotive force (EMF) around the loop. By itself this would drive a circulating current which would be extremely large due to the small electron mass. Note that even if large electrostatic fields in the plasma arise (indeed also driven by the pressure gradient), they integrate to zero around the loop. Therefore, absent inductive electric fields, a large circulating current would be driven. However, the increasing circulating current creates an increasing magnetic field, which induces an electric field by Faraday's law, which can balance the Biermann EMF. From this balance one obtains $\partial \mathbf{B} / \partial t = \nabla \times (\nabla p_e/n_e)$, which is the standard result. The only subtlety in the final equation is that the causal role of the electrons currents in driving the magnetic field is hidden. Mathematically this is because in the Ohm's law, \mathbf{j} is finite, but $m_e \mathbf{j}$ is small compared to \mathbf{E}_{ind} and $\nabla p_e/n_e$ due to the small electron mass. (With a little more analysis, the precise criterion for ignoring the electron inertia term is for density and temperature gradient scales larger than the electron skin depth, in which case the energy in Biermann magnetic fields dominates the kinetic energy in electron flows.)

We analyze the development and evolution of the magnetic field using the generalized Ohm's law implemented in the PSC code, which takes a slightly different form than Eq. 1,

$$\mathbf{E} = -(\mathbf{v} \times \mathbf{B}) + \frac{1}{n_e e} (\mathbf{j} \times \mathbf{B}) - \frac{\nabla p_e}{n_e e} - \frac{1}{n_e e} \nabla \cdot \Pi - \frac{1}{n_e e} \mathbf{R}_{ei}. \quad (5)$$

The terms on the RHS are: the ion flow term; Hall term; electron pressure term, which can drive the Biermann effect; electron pressure tensor, which embodies momentum transport; and collisional momentum exchange. Here we separate the pressure scalar and pressure tensor from the total stress tensor, by defining the pressure tensor as trace-less. The collisional momentum exchange \mathbf{R}_{ei} includes both resistive diffusion and the Nernst-effect (via the thermal force). It is obtained by diagnosing the total momentum exchange between electrons and ions during the collision subroutine. This provides a rigorous measure of the momentum exchange and confirmation of total momentum conservation, but does not allow ready separation of the diffusion and Nernst effects, which requires extra analysis.

A. Simulation setup and parameters

Using the model described above we simulate the magnetic field generation and evolution of recent laser plasma experiments on magnetic reconnection. The experiments were conducted at Vulcan and Shenguang-II laser facilities. (The experiments on OMEGA of Li *et al.* [30] and Rosenberg *et al.* [33] are very large in (L/d_{i0}) and will be considered in future work.) Both experiments coupled several hundred J of laser energy onto thin metal targets with laser intensities near 10^{15} W/cm², producing

TABLE I. Parameters for Vulcan [29] and SG-II [31, 55] reconnection experiments

	Vulcan	SG-II
Input:		
Ions	Al ¹³⁺	Al ¹³⁺
n_{ab} (m ⁻³ , DRACO)	5×10^{26}	4.5×10^{27}
T_{ab} (eV, DRACO)	1500	2000
heating radius R_H (μm)	50	100
Separation $2L$ (μm)	400	400
Dimensional:		
d_{e0} (μm)	0.24	0.08
d_{i0} (μm)	14	4.8
C_{s0} (m/s)	2.7×10^5	3.2×10^5
$t_d = d_{i0}/C_{s0}$ (ps)	52	15
$B_0 = (\mu_0 n_{ab} T_{ab})^{1/2}$ (T)	380	1300
$B_0 d_{i0}$ (T-mm)	5	6
ω_{ce0} (ps ⁻¹)	70	230
ν_{ei0} (ps ⁻¹)	2.7	14
Dimensionless:		
R_H/d_{i0}	2	15
L/d_{i0}	12	40
λ_{mfp0}/d_{e0}	25	15

TABLE II. PSC Simulations for Vulcan [29] and SG-II [31, 55] reconnection experiments

	Vulcan	SG-II
Initialization:		
R_H/d_{i0}	2	12
L/d_{i0}	12	40
λ_{mfp0}/d_{e0}	30	20
Results:		
t_{coll}/t_d	5–10	15–20
Max $\Psi / B_0 d_{i0}$	3	3

high temperature ($T \sim 1$ keV), and high-density plasmas ($n \sim 10^{25}$ m⁻³).

DRACO RH simulations were conducted to predict the plasma temperature T_{ab} and density n_{ab} to determine the parameters for PSC simulations using the scheme above. The simulations used quoted laser intensities $I \sim 10^{15}$ W/cm², laser-incidence angles (45 degrees in both cases), and then Aluminum foils as the target material. Table III summarizes the results of these calculations and presents the resulting dimensional parameters (n_{ab}, T_{ab}, t_d, B_0) for converting the PIC results back to physical units.

B. Simulation Results

These PSC simulations represent the first kinetic simulations of Biermann battery magnetic field generation in plasmas with parameters and geometry directly matched to these recent laser experiments. The simulations further show the advection processes governing the magnetic field evolution, and resulting magnetic field compression and current sheet formation when two neighboring plumes collide. The simulations also reveal novel physics which has not been previously reported, such as the role of the Hall effect for fast magnetic field advection over the target surface. Table II summarizes the dimensionless parameters used for the simulations as well as numerical details, and typical results such as peak magnetic field strengths, and time for collision of a significant magnetic field for two plasmas initially separated by the distance $2L$.

Figure 3 shows the plasma density and magnetic field evolution at three characteristic times of the simulation modeling the experiments of Ref. [29]. The left panel shows the initial condition with a thin high-density target surrounded by a low-density ambient plasma, and zero magnetic field. This plasma is heated with a gaussian heating profile with $1/e$ radius of $2d_{i0}$. The plume quickly reaches the ablation temperature T_{ab} within the heated region and expands. The evolution from $t = 0$ to $t = 2.15t_d$ shows the generation of Biermann magnetic fields near the target surface, produced in the regions with non-collinear density and temperature gradients in the laser-heating area, which subsequently expand vertically as well as radially outward.

Notably, peak magnetic fields up to $0.3 B_0$ are rapidly generated, which correspond to magnetic fields of order 1 MG, making use of the scalings of Table I. Second, a leading edge of magnetic field has been generated and advected approximately $10 d_{i0} \approx 200$ μm in $t = 2t_d \approx 100$ ps, for magnetic advection rate of approximately 5 times the sound speed C_{s0} , or roughly 2×10^6 m/s. This fast expansion speed corresponds to a small leading edge of magnetic field, and is qualitatively (but not quantitatively) consistent with an extremely fast expansion inferred in some experiments at up to 8×10^6 m/s [44]. We note that this leading edge of the magnetic field is fairly small compared to the total magnetic flux, which is carried over a longer timescale of $4\text{--}5 t_d$, corresponding to speeds near $2\text{--}2.5 C_{s0}$. Line-integrated magnetic fields $\int B_y dz$ of order $3B_0 d_{i0} \approx 15$ T-mm, (or 150 MG- μm , in a common unit scheme) are obtained, in reasonable agreement with typical magnetic fields inferred in laser-plasma experiments [6, 29].

The particle-in-cell simulation allows the full dynamics of the magnetic fields to be tracked using the generalized Ohm's law. Figure 4 shows plots of all terms of the Ohm's law versus space at the characteristic time $t = 2.15t_d$ when the magnetic field has expanded a significant distance over the target surface. The top-left panel shows $\partial B_y / \partial t$ (with units B_0/t_d) directly observed from

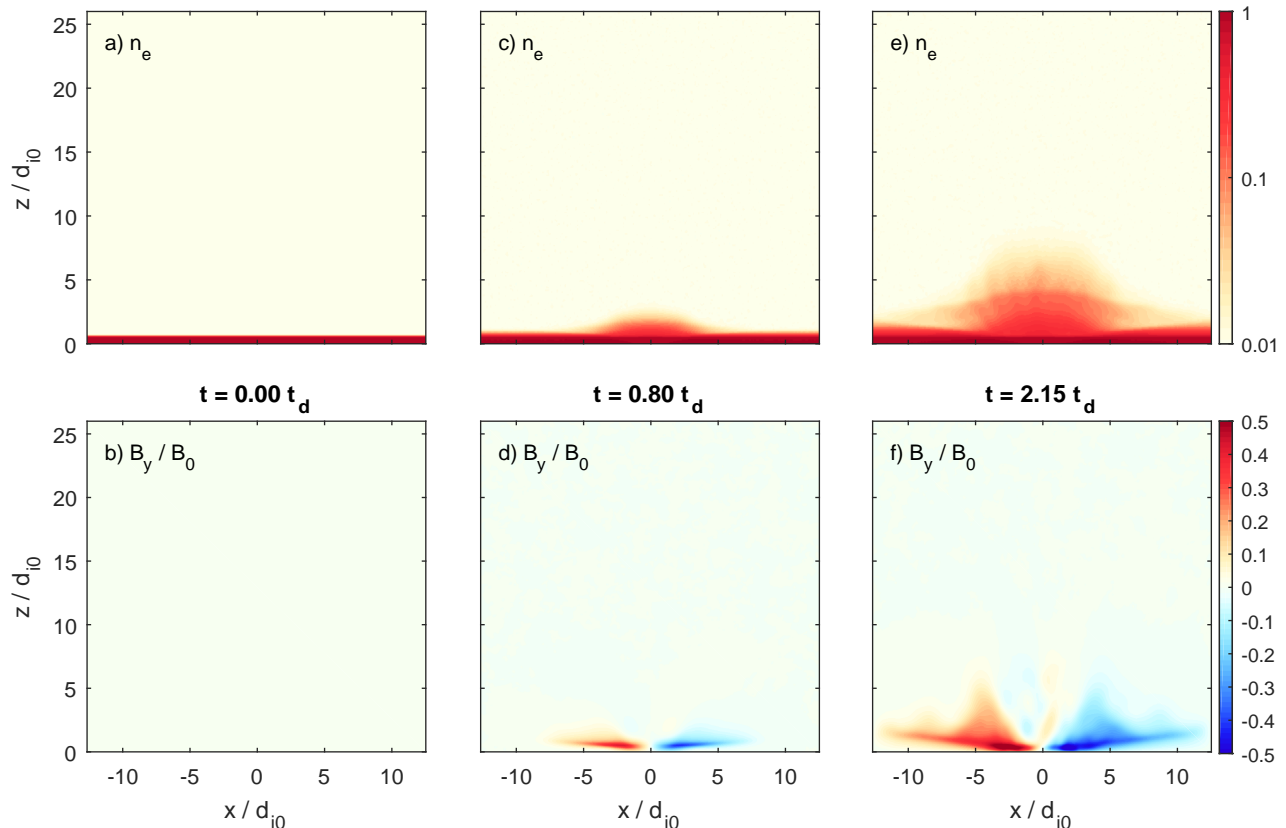


FIG. 3. Evolution of plasma density and magnetic field in a simulation model of the experiments of Ref. [29].

the field evolution in the simulation, whereas the panel below it shows the *inferred* evolution by taking the curl of the measured Ohm’s law, summing all measured effects. These measured effects are broken down into: the Biermann term; ion advection ($\text{curl } \mathbf{V} \times \mathbf{B}$); the Hall term ($\text{curl } (1/ne) \mathbf{j} \times \mathbf{B}$); collisional momentum exchange (\mathbf{R}_{ei}); and the pressure tensor. These terms are summed to produce \mathbf{E}_{Ohm} , the curl of which is plotted in the bottom left panel. The excellent agreement between the observed field evolution and curl of Ohm’s law indicates that all field evolution effects are accounted for. We now briefly describe the role of these terms.

First, at this time the Biermann term continues to operate and is dominant near the regions of strong radial temperature gradient, near $x = \pm 5d_{i0}$ (Fig. 4e). The hotspot has also spread due to thermal transport, leading to “advected” Biermann generation outside of the initial heating radius ($R_H = 2d_{i0}$). We also quantify magnetic field advection by multiple effects. We observe a strong outward-radial advection from the Hall term (Fig. 4d), which has a characteristic “advection” pattern $\partial B/\partial t \sim \nabla \times (v \times B)$; for example, for $x > 0$, we observe $\dot{B}_y > 0$ at $x = 5d_{i0}$ and $\dot{B}_y < 0$ at $x = +10d_{i0}$, which transports the negative B_y outward. This shows a fast radial advection due to the Hall effect, an effect which has not previously been documented to drive a fast

radial expansion. The Hall effect results from the differing electron and ion flows associated with magnetic fields with gradients on the local ion-skin-depth scale near the target surface. Meanwhile, an advection pattern is also observed due to ion flow (Fig. 4c), however it predominantly transports the magnetic field vertically off the target surface. The simulation also tracks the momentum exchange term. This term contains both advection from the Nernst term (also known as the thermal force) and collisional diffusion. However, we note that in this simulation, the pattern is consistent with diffusion and destruction of magnetic field rather than advection; that is, the signs of R_{ei} are such to locally decrease the magnetic field everywhere, rather than bipolar signatures consistent with transport.

Finally, we note that due to finite collisionality in the simulation, we do not observe an electron Weibel instability, as has been observed in collisionless simulations in the same large L/d_e regime [53]. However, we do observe *ion*-Weibel instability [7] due to interaction of the expanding plasma with the background plasma. In this simulation, at relatively small R_H/d_{i0} , a single Weibel filament grows in this simulation at the core of the bubble for $|x| < 2d_{i0}$, at $z = 5d_{i0}$. A trace of Weibel instability in the expanding plasma is reflected in the alternating pattern of the electron pressure tensor (Fig. 4f) near

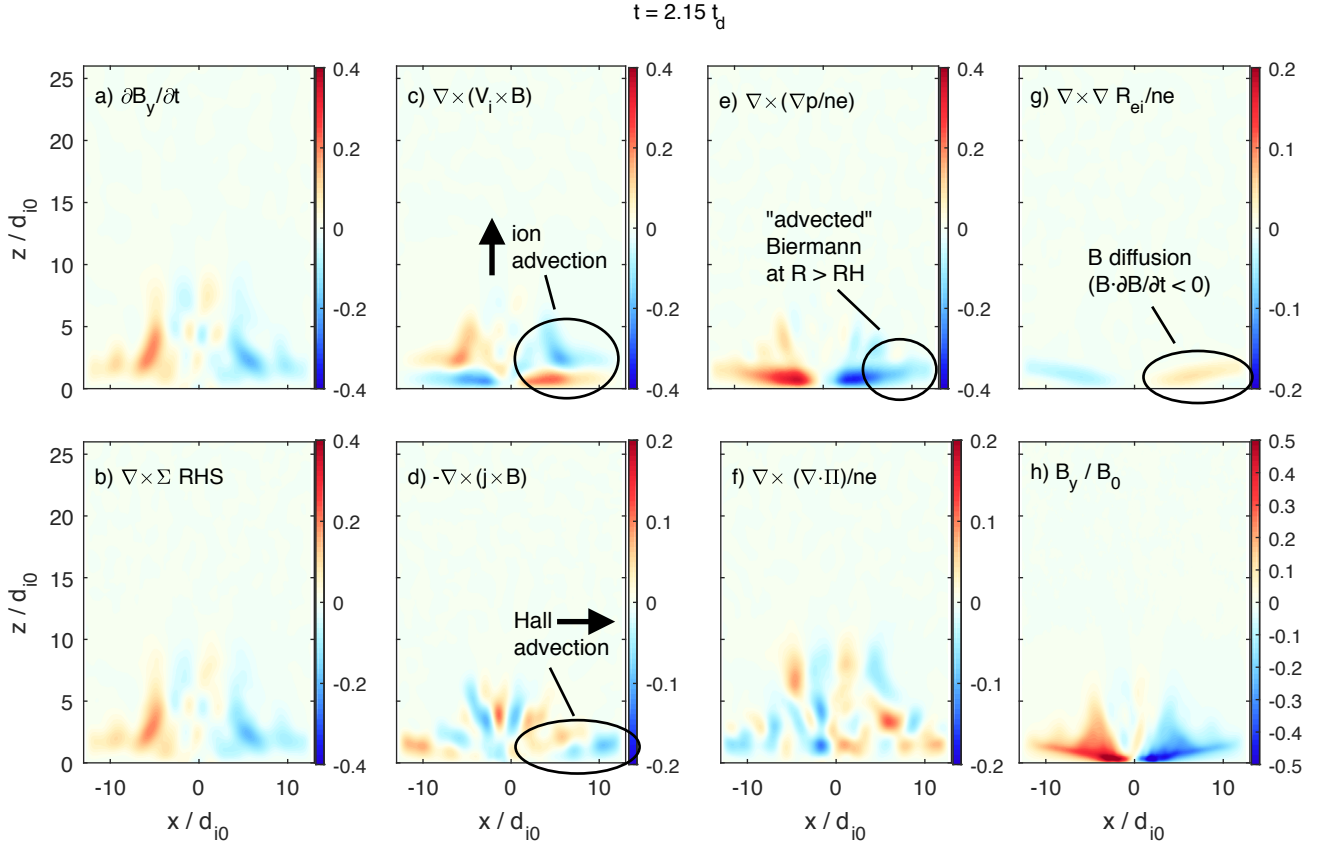


FIG. 4. Analysis of all terms of the Ohm's law for the magnetic field evolution in simulations of the Vulcan experiments [29].

$z = +5d_{i0}$.

Simulations of colliding plasmas are conducted by moving the boundary so that two plumes are centered, respectively, at the boundaries $x = \pm L$, which then evolve and collide at $x = 0$. A current sheet forms as the opposite fields from the two plasmas interact and compress, showing from first principles how and where a current sheet forms for Biermann-battery based magnetic reconnection experiments. Figure 5 shows current sheet formation process and analysis by the Generalized Ohm's law. The 2-D magnetic field profiles at the characteristic time of current sheet formation for both Vulcan (Fig. 5c) and SG-II experiments (Fig. 5e), provides a comparison of the magnetic field produced for the two systems, which differ primarily in the system size parameters L/d_{i0} and R_H/d_{i0} . For Vulcan, compressed magnetic fields in the current sheet $B_y \approx 0.3B_0$ are obtained through much of the plume, whereas for SG-II typical magnetic fields in the plume itself are near $0.1 B_0$, but there is a flux compression up by a factor ≈ 3 in the collision region leading to peak fields again near $0.3 B_0$. The larger B field in the Vulcan case (scaled to B_0 , though not in physical units) is due to the smaller $(L, R_H)/d_{i0}$, consistent with typical Biermann scaling [53].

Figure 5(a,c) show quantitative comparison of the line-integrated magnetic field $\int \mathbf{B} \times d\ell = \int B_y dz$,

which is useful for comparison with experimental proton-radiography measurements [6, 33], which produce maps of the line-integrated fields. We obtain $\int B_y dz$ in the range of 1–3 $B_0 d_{i0}$ for the two experiments, which corresponds to experimental values in the range of 5–15 T-mm. In the case of the SG-II experiments, we note the simulation observes a flux compression and stacking into the current layer, such that $\int B_y dz$ peaks by about 30% in the reversal region compared to immediately upstream. This demonstrates that the magnetic field is significantly modifying the hydrodynamic evolution.

Figure 5(b,d) analyzes the terms driving the evolution of $\int B_y dz$, namely that the evolution of line-integrated magnetic field is driven by the line-integrated Ohm's law, $(\partial/\partial t) \int B_y dz = \int (\nabla \times E)_y dz$. This shows which terms are playing the greatest role on average in evolving the magnetic flux, which is valuable given the richness of physics demonstrated in Fig. 4. First, the red and blue curves are the directly measured $\partial B_y/\partial t$ and summed terms of Ohm's law, demonstrating excellent agreement and that all effects have been measured. The bi-polar enhancement of $\partial B_y/\partial t$ near $x = 0$ is consistent with a current sheet that is still compressing and thinning. The black curves show the Biermann term, which peak in the Biermann-generation regions in the core of the bubbles near regions of large temperature gradients. (Again, the

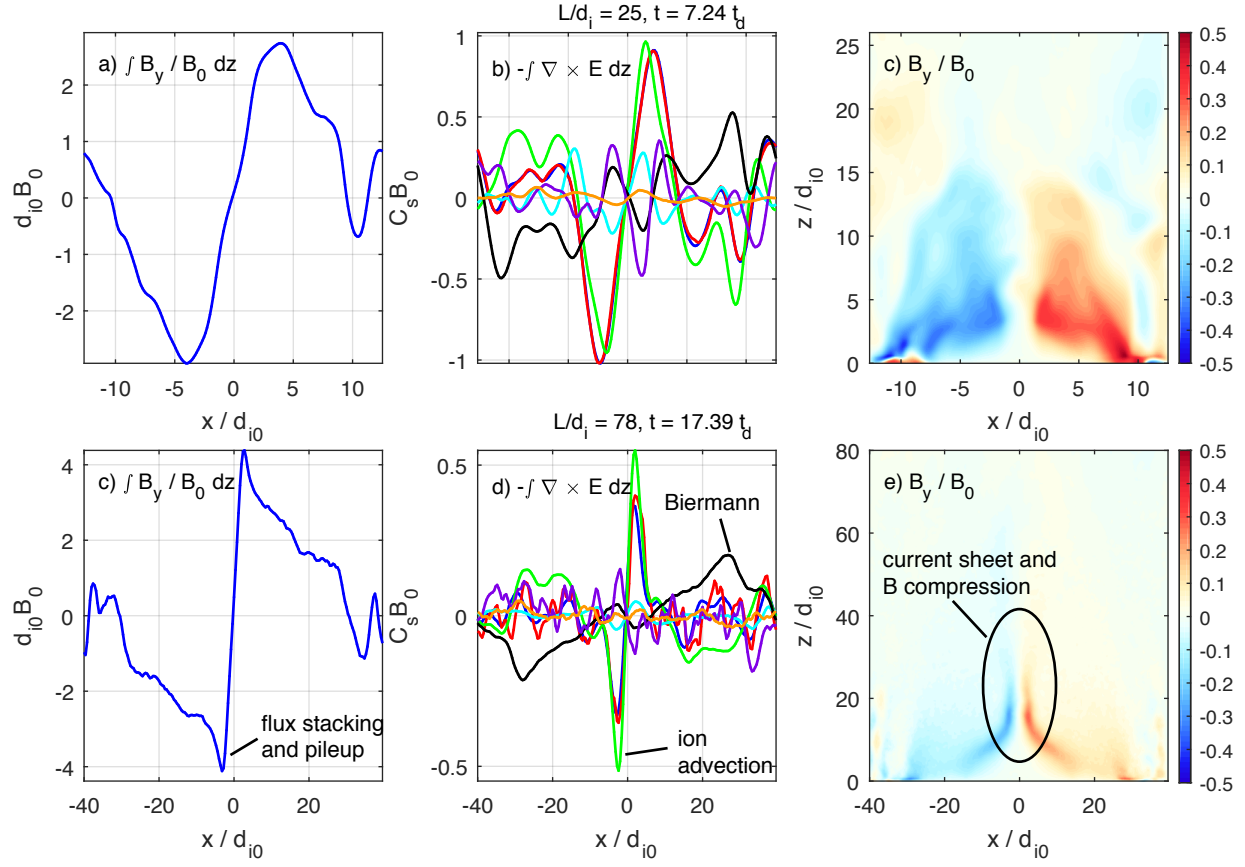


FIG. 5. Analysis of the evolution of magnetic fields in the simulations of Vulcan [29] and SG-II [31, 55] experiments. (a,d) Line-integrated magnetic fields, (b,e) vertically-integrated curl of Ohm's law showing the contributions to magnetic flux evolution. (c,f) 2-D magnetic field profiles showing current sheet formation when two plumes collide.

discussion here is for vertically-integrated quantities; for brevity we will not mention this each time.) We note there is a greater spatial separation between Biermann generation region and the current sheet in the SG-II case, because the greater L/d_{i0} . The green curve shows the ion flow, which dominates in advecting magnetic field away from the Biermann formation regions and into the forming current sheet. The light-blue curve is the Hall term which plays a role to advect the magnetic field into a narrower current sheet than the ion term alone. The purple curve shows magnetic field destruction by the off-diagonal pressure term. The orange term shows a small amount of magnetic field destruction by collisional diffusion, which is also largely negligible.

The simulations here demonstrate how the flows generate field and advect it toward the collision region, showing for the first time the details of the formation of a current sheet where \mathbf{B} reverses over a narrow layer. A follow-up paper will analyze the subsequent magnetic reconnection, which requires full 3-D simulations to allow reconnection outflows [39].

IV. FORMATION OF MAGNETIZED COLLISIONLESS SHOCKS

Shockwaves in space and astrophysical plasmas occur where plasmas interact at super-sonic or super-magnetosonic velocity [14, 56–58]. In collisionless plasmas the shock layer forms at kinetic plasma scales through collective electromagnetic effects, which convert the flow energy to heat and accelerate non-thermal particle populations, [15, 59], including cosmic rays [60–62]. Of particular importance are the class of supercritical shocks [63] ($M \gtrsim 3$), which propagate faster than can be accommodated by entropy production in the shock, and therefore reflect significant numbers of particles back into the upstream, seeding proposed cosmic ray acceleration processes [40, 64–66] such as diffusive shock acceleration (DSA). Spacecraft routinely observe shocks both at planetary bow shocks, and embedded in solar wind flows. Recent spacecraft such as MMS produce detailed high-resolution data sets of collisionless shock crossings [67]. Nonetheless, controlled, repeatable laboratory experiments offer opportunities to study aspects which are challenging with single- or few-spacecraft shock crossings, including higher-dimensional and temporal effects such as rippling instabilities and shock reformation, and particle energization by shocks.

Recent laboratory experiments have demonstrated the generation of shocks in magnetized plasmas driven by laser-driven pistons both in a low-Mach-number ($M_A \sim 2$) regime [34, 68], and in a high-Mach-number regime ($M_A \sim 15$) [35]. We briefly review the opportunities for laboratory experiments. First, laboratory experiments may allow investigation of higher dimensional stability and dynamics of shocks beyond standard 1-D quasi-steady shock theories. One manifestation of this is the

reformation process of the shock, where the “foot” of reflected ion gradually grows until it disrupts the shock, leading to formation of a new shock at the location of the erstwhile ion foot. Non-stationarity has been observed in 1-D plasma wind tunnel experiments [69]. A related process is transverse rippling of the shock front by instabilities [70–72]. At extreme mach number ($M_A \sim 40$) the front becomes turbulent by counterstreaming Weibel instability [40], which is very interesting as these instabilities may be help energize particles near the shock front and inject them into DSA [71, 72]. While some of these processes have been documented recently by spacecraft [67, 73], in general this is difficult with single- or few-spacecraft crossing but it is readily possible with imaging diagnostics available in laboratory experiments.

Second, shock acceleration is believed to be very important in astrophysical plasmas, and there is strong evidence for particle acceleration near to shocks— for example the TeV synchrotron emission [15] and pion decay signatures conclusively demonstrate electrons and cosmic ray protons are accelerated in blastwaves of supernova remnants [62]. However, very little can be constrained about the shock environment and acceleration process from these remote sensing observations. While local spacecraft observations have demonstrated particle acceleration near shocks [59], laboratory experiments can contribute significant understanding of shock acceleration through parametric studies of the dependence of acceleration mechanisms on plasma and shock parameters. Of particular importance is the physics and efficiency of the “injection” process by which particles obtain a pre-acceleration which enables them to then participate in the DSA.

A recent series of experiments have developed a new platform to study the physics of high Mach-number flows, including magnetized shocks and reconnection, in the laboratory [32, 35]. These experiments, conducted at the OMEGA EP facility at the University of Rochester Laboratory for Laser Energetics, demonstrated how to generate controlled supersonic ablation flows into a pre-magnetized ambient plasma. The hallmark of the platform is that externally-controlled magnetic fields are generated by a compact pulsed power system [74], generating field of order 10 T over a volume several-mm on a side, which is used to create a pre-magnetized ambient plasma as a medium for magnetized shocks and flows.

In this section we extend the kinetic ablation simulations of the previous sections to study plasma expansion into a magnetized background plasma to model this experimental system. Kinetic simulations played an essential role in developing this experimental platform by providing intuition on the behavior of the system over broad parameter regimes, and by pointing out experimental observables. Recently published simulations with this model have shown how the expanding plasma sweeps up the ambient plasma and field, leading to flow and density steepening and magnetic compression, the onset of ion-reflection, and finally the formation of a magnetized

TABLE III. Parameters for OMEGA-EP magnetized plume experiments

Input:	
n_{ab} (m^{-3} , DRACO)	6×10^{26}
n_{bg} (m^{-3})	6×10^{24}
T_{ab} (eV, DRACO)	800
heating radius R_H (μm)	350
heating exponent κ	4
Dimensional:	
d_{e0} (μm)	0.24
$d_{i0,CH}$ (μm)	14
C_{s0} (m/s)	2×10^5
$B_0 = (\mu_0 n_{ab} T_{ab})^{1/2}$ (T)	300
B_{up} (T)	8
$t_d = d_{i0}/C_{s0}$ (ps)	52
$\omega_{cH,up}^{-1}$ (ns)	1.3
$\omega_{cC,up}^{-1}$ (ns)	2.6
ω_{ce0} (ps^{-1})	50
ν_{ei0} (ps^{-1})	4
Dimensionless:	
R_H/d_{i0}	30
λ_{mfp0}/d_{e0}	12
B_{up}/B_0	.025
n_{bg}/n_{ab}	.01

high-Mach number shock [35]. A slight variant of the model, which using a particle source term rather than a heating operator, was used to simulate the reconnection experiments in Ref. [32], which showed important features of the experiments including flow stagnation of two colliding plasmas at the ion-skin-depth scale, and current sheet tearing during the strongly-driven magnetic reconnection. Here we describe the computational model and parameters in detail and show new results of these processes obtained with large-scale 2-D shock simulations.

A. System setup and parameters

DRACO radiation-hydrodynamics simulations are again used to provide plasma parameters to drive the PSC ablation simulations. Table III lists the relevant ablation parameters predicted by DRACO, which used the laser geometry and parameters of the experiments [32, 35], including the highly oblique laser-incidence, 74° , and the EP 750- μm distributed phase plate, which generates a smooth beam profile with $1/e$ radius $R_H = 340 \mu\text{m}$ and a 4th-order super-gaussian profile (laser intensity $I \propto \exp[-(r/R_H)^\kappa]$, with $\kappa = 4$). We take an upstream magnetic field near 8 T, and an upstream density of $6 \times 10^{24} \text{m}^{-3}$, which is somewhat above typical DRACO predictions and recent measurements, but was

TABLE IV. PSC Shock Simulations

Input:	
R_H/d_{i0}	30
λ_{mfp0}/d_{e0}	50
B_{up}/B_0	0.04
n_{bg}/n_{ab}	0.01
Electron-scale parameters:	
M_i/m_e	100
$m_e c^2/T_{e,ab}$	16
Results:	
$t_{shock}\omega_{ci,up}$	~ 1
V_{shock}/C_{s0}	4.5

used as part of a scan to confirm shock formation for a variety of upstream densities. The plasma ablated from the targets is a 60-40 mixture of hydrogen and carbon (C^{6+}) for which DRACO uses an average ion model.

For the present paper, we consider an “equivalent” kinetic PSC simulation based on a single species. By this we mean that the ion-scale parameters are chosen to match Table III, but are used in a simulation with only H+ ions, for simplicity. Ablation timescales ($t/t_d, t\omega_{ci,up}$) and length scales (x/d_{i0}) are measured in the pure PSC simulation in relation to this lone species. Extension to multiple species in the kinetic simulation is straightforward, and in fact was used in Schaeffer *et al.* [35] for accurate comparison with the experiment, and will be considered in more detail in future work. Parameters for the present simulations are presented in Table IV. We note that in addition to the single ion species, we use slightly increased magnetic fields B_{up}/B_0 to obtain faster shock formation in a given simulation wall time, and we use lower electron collisionality $\lambda_{mfp0}/d_{e0} \approx 50$ than estimated for the experiments. The plasma ablation flows in this PSC simulation and DRACO are compared in Fig. 2, where the good agreement of the two flows supports the scaling via the ion-scale parameters between these two very different simulation codes.

B. Results

Figure 6 shows the results of large-scale 2-D simulations on the expansion into the background plasma and generation of the magnetized shock. The upper (a-c) and lower (d-f) panels show the evolution at two characteristic times, near the time of initial shock formation ($t\omega_{ci,up} = 0.9$, a-c) and later as the shock completely separates from the piston ($t\omega_{ci,up} = 1.9$, d-f). We scale the time evolution in units of $t\omega_{ci,up}$ based on the initial upstream ambient field, as we have found that this is the most relevant time-scale for shock formation for a wide range of $t_d\omega_{ci,up} \sim \beta^{-1/2}$. The left panels (a,d) show the plasma density evolution, which show the density compression that forms as the ablation plasma

flows into and compresses the ambient plasma, initially at $n_{bg} = 0.01n_{ab}$. The interaction of the two plasmas occurs where the exponential ablation plume and background plasma density approximately coincide. Because of the ambient magnetic field, the plasmas cannot fully interpenetrate, and instead the field and plasma are swept up, and steepen into a shock. At late times (Fig. 6d), the shock ramp separates from the piston, forming a characteristic “double-jump” of the density. This feature was in fact predicted first from PSC simulations and was used as an experimental observable of the shock formation in experiment, where the transition over time from single to double-density jumps are observed with interferometry [35]. This shows the value of kinetic simulations in interpreting experiments.

Figure 6(b,e) show the magnetic field evolution in the simulations. Initially the upstream magnetic field lies in the simulation plane and is a uniform field of magnitude B_{up} . However, this field is swept up and compressed into the ablation flow. The in-plane magnetic flux is conserved, such that the magnetic field compressed into the shock is exactly that expelled from the diamagnetic cavity near the targets. Over time, the amount and magnitude of the magnetic expulsion increases, and these ablation-driven shocks continue to expand through the whole simulation. The magnetic field compresses to a value of about $6 B_{up}$ by $t\omega_{ci,up} = 1.9$.

Meanwhile, Fig. 6(c,f) shows additional magnetic field *generated* near the shock by the plasma. This magnetic component is the out-of-plane (azimuthal in a toroidal geometry) and is not present in the initial condition, but as shown in the previous section is readily generated by a variety of processes. We note first of all the Biermann field generation near the target, which is analogous to the pure Biermann generation in unmagnetized expansions shown previously in Fig. 3. Perhaps unsurprisingly, the Biermann field is also swept up by the plasma and compressed into the shock. However, we note that the Biermann field is far from uniform in polarity, and shows regions of both signs depending on the polar location within the shock. Fields of the same sign as the standard Biermann fields are generated in equatorial regions (near the target surface), but regions with opposite polarity are generated at oblique polar angles. We refer to these as “shock Biermann” fields, as this is kinetic Biermann field generation within a collisionless shock. We believe this is the first evidence for this process which should be considered more broadly in astrophysical and laboratory shocks. Furthermore, the field quantitatively modifies the magnetic fields in the shock, with $B_{Biermann} \sim 3B_{up}$ reaching approximately 50% of the compressed shock field $B_{shock} \sim 6B_{up}$ under the present parameters. The Biermann fields within the shock can quantitatively (or even qualitatively, if the upstream field is weak enough) modify shock formation via enhancing particle reflection. This topic is the subject of ongoing studies.

Finally, near the poles, the simulations also show the development of out-of-plane filamentary fields character-

istic of Weibel instability [7], both upstream and downstream of the shock. The upstream Weibel is a transverse instability of the reflected ions kicked forward into the upstream plasma, whereas the downstream Weibel results from ablated ion gyration off the compressed fields, returning into the downstream. Weibel instability has been proposed to enhance particle energization in high-Mach number shocks [40]. These simulations therefore show the interaction of this instability with scaled laboratory shocks, and suggest that both these processes may be observable in laboratory experiments.

V. DISCUSSION AND CONCLUSIONS

In this paper, we have developed fully kinetic simulation techniques to model recent laser-plasma experiments on laboratory astrophysics, allowing simulation of a variety of phenomena relevant to astrophysical plasmas within a common framework.

First, we set out an overall methodology based on dimensionless parameters for designing scaled simulations to model these processes. Ion-scale dimensionless parameters are derived and provide a basis to initialize the simulations with relevant parameters to match experiments. This is important because for fully kinetic simulations over these plasma length scales ($L/d_i \sim 100$), evolving for multiple sound crossing times ($tC_s/L \gtrsim 1$), it is still not computationally practical to match all the dimensionless parameters of the system, especially those involving the small electron mass (M_i/Zm_e), and the speed of light ($m_e c^2/T_e$). We note that kinetic simulations with reduced parameters like those shown here are very common in dedicated simulations of magnetic reconnection [21, 36, 43] and shocks [13, 40]; here this technique is extended to general ablation flows for this whole family of phenomena. These dimensionless parameters also provide a basis to scale the results to astrophysical plasmas. Some limitations of the present model include the fact that the target does not reach up to solid densities, and the lack of a laser-ray-trace energy-deposition model which requires input from a separate radiation-hydrodynamics simulation. Both of these limitations may be improved by further code development. However, already the model is in general agreement with the expanding plasma evolution of DRACO.

Subsequently, we showed how the kinetic ablation model is used to simulate two sets of recent laser-driven laboratory astrophysics experiments. First, we consider the Biermann battery magnetic field generation in recent experiments with single and multiple expanding plumes. The simulations results are directly analyzed via the generalized Ohm’s law and show both the location and time of Biermann-battery field generation, and the mechanisms (ion flows, Hall flows) which advect these fields and form a current sheet when two neighboring plumes collide. The compression of the field indicates that the magnetic field has modified the hydrodynamic evolution

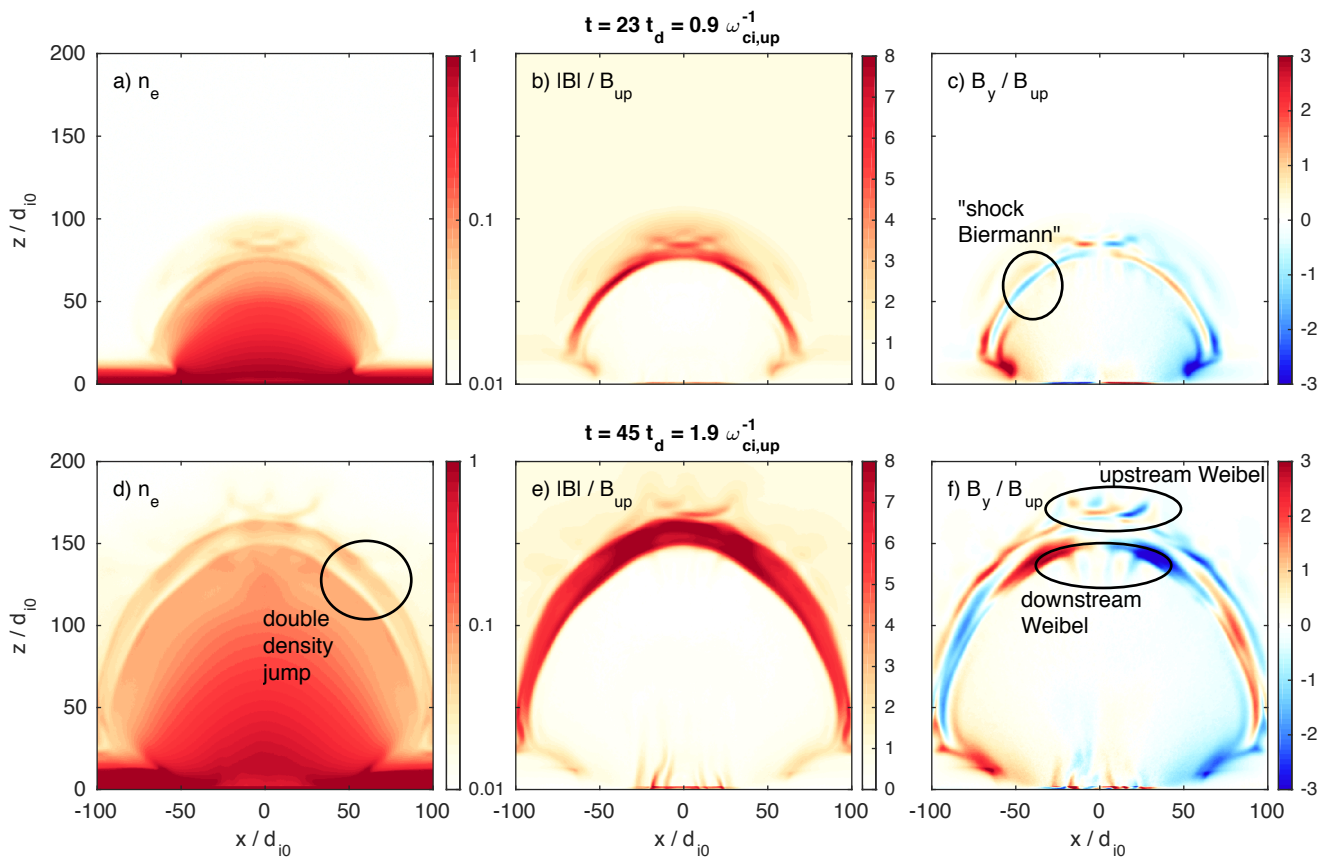


FIG. 6. Generation of magnetized shocks by ablation flow into a magnetized ambient plasma, at two times characteristic of shock formation, $t\omega_{ci,up} = 0.9$ (a-c) and $t\omega_{ci,up} = 1.9$ (d-f). (a,d) 2-D density maps; (b,e) total magnetic field $|B|$ emphasizing the compression of the initial upstream field and formation of the diamagnetic cavity. (c,f) shows the additional out-of-plane field generation B_y in the 2-D expansion by the Biermann effect, shock-Biermann, and Weibel instability.

of the two plasmas. The 2-D simulations shown here do not include the magnetic reconnection phase of the experiments, which requires a 3-D simulation, but such simulations are underway and will be reported in a separate publication. The results provide insights into the evolution of ablated plumes of wide applicability in laboratory plasmas and provide insights for designing experiments and interpreting results on magnetic reconnection, including rates of magnetic reconnection and efficiency of acceleration of particles.

Finally, we extended the simulation to study plasma expansion into a pre-magnetized background plasma, modeling recent experiments on magnetic reconnection and collisionless shock formation. The simulations provide important insights for interpreting the experiments, including confirmation of the formation of shocks on the timescale $\omega_{ci,up}^{-1}$. These large-scale 2-D simulations also show the development of Biermann battery magnetic fields within the collisionless shock front, which quantitatively modify the (compressed) shock fields, as Biermann fields in the shock up to about 50% of the compressed shock fields are generated. We note that the development of Biermann fields in collisional, MHD-scale

shocks was considered recently in Ref. [26], which presented analytic arguments for the magnitude and sign of the magnetic field, with proposed prescriptions of how to model them in reduced fluid models. A comparison between kinetic and MHD simulations is potentially of great value in benchmarking these reduced models. The simulations also show the development of transverse Weibel instability both ahead and behind the shock, driven in the first case by the typical forward particle reflection off the shock at high Mach-number, and behind the shock by backward gyration or rebound of the piston ions off the magnetic compression. The results provide insights which will help design future experiments on transverse shock stability and particle acceleration by shocks.

ACKNOWLEDGMENTS

Simulations were conducted on the Titan supercomputer at the Oak Ridge Leadership Computing Facility at the Oak Ridge National Laboratory through the Innovative and Novel Computational Impact on Theory and Experiment (INCITE) program, which is supported by

the Office of Science of the DOE under Contract No. DE-AC05-00OR22725. This research was also supported

by the DOE under Contracts No. de-sc0008655 and No. de-sc0016249.

-
- [1] D. D. Ryutov, R. P. Drake, and B. A. Remington, *The Astrophysical Journal Supplement Series* **127**, 465 (2000).
- [2] E. Buckingham, *Physical Review* **4**, 345 (1914).
- [3] J. A. Stamper, K. Papadopoulos, R. N. Sudan, S. O. Dean, E. A. McLean, and J. M. Dawson, *Physical Review Letters* **26**, 1012 (1971).
- [4] J. A. Stamper, E. A. McLean, and B. H. Ripin, *Physical Review Letters* **40**, 1177 (1978).
- [5] M. A. Yates, D. B. van Hulsteyn, H. Rutkowski, G. Kyrala, and J. U. Brackbill, *Physical Review Letters* **49**, 1702 (1982).
- [6] R. D. Petrasso, C. K. Li, F. H. Séguin, J. R. Rygg, J. A. Frenje, R. Betti, J. P. Knauer, D. D. Meyerhofer, P. A. Amendt, D. H. Froula, O. L. Landen, P. K. Patel, J. S. Ross, and R. P. J. Town, *Phys. Rev. Lett.* **103**, 085001 (2009).
- [7] W. Fox, G. Fiksel, A. Bhattacharjee, P. Y. Chang, K. Germaschewski, S. X. Hu, and P. M. Nilson, *Physical Review Letters* **111**, 225002 (2013).
- [8] C. M. Huntington, F. Fiuza, J. S. Ross, A. B. Zylstra, R. P. Drake, D. H. Froula, G. Gregori, N. L. Kugland, C. C. Kuranz, M. C. Levy, C. K. Li, J. Meinecke, T. Morita, R. Petrasso, C. Plechaty, B. A. Remington, D. D. Ryutov, Y. Sakawa, A. Spitkovsky, H. Takabe, and H. S. Park, *Nature Physics* **11**, 173 (2015).
- [9] Manuel, C. K. Li, F. H. Séguin, J. Frenje, D. T. Casey, R. D. Petrasso, S. X. Hu, R. Betti, J. D. Hager, D. D. Meyerhofer, and V. A. Smalyuk, *Physical Review Letters* **108** (2012), 10.1103/physrevlett.108.255006.
- [10] L. Gao, P. M. Nilson, I. V. Igumenshev, S. X. Hu, J. R. Davies, C. Stoeckl, M. G. Haines, D. H. Froula, R. Betti, and D. D. Meyerhofer, *Physical Review Letters* **109**, 115001 (2012).
- [11] R. M. Kulsrud, R. Cen, J. P. Ostriker, and D. Ryu, *The Astrophysical Journal* **480**, 481 (1997), arXiv:astro-ph/9607141.
- [12] M. V. Medvedev and A. Loeb, *The Astrophysical Journal* **526**, 697 (1999), arXiv:astro-ph/9904363.
- [13] T. N. Kato and H. Takabe, *The Astrophysical Journal Letters* **681**, L93 (2008).
- [14] E. J. Smith, L. Davis, D. E. Jones, P. J. Coleman, D. S. Colburn, P. Dyal, and C. P. Sonett, *Science* **188**, 451 (1975).
- [15] A. Bamba, R. Yamazaki, M. Ueno, and K. Koyama, *The Astrophysical Journal* **589**, 827 (2003).
- [16] M. Øieroset, R. P. Lin, T. D. Phan, D. E. Larson, and S. D. Bale, *Physical Review Letters* **89**, 195001 (2002).
- [17] J. F. Drake, M. Opher, M. Swisdak, and J. N. Chamoun, *The Astrophysical Journal* **709**, 963 (2010).
- [18] M. Yamada, R. Kulsrud, and H. Ji, *Reviews of Modern Physics* **82**, 603 (2010).
- [19] E. M. Epperlein and M. G. Haines, *Physics of Fluids* **29**, 1029 (1986).
- [20] M. G. Haines, *Plasma Physics and Controlled Fusion* **28**, 1705 (1986).
- [21] J. Birn, J. F. Drake, M. A. Shay, B. N. Rogers, R. E. Denton, M. Hesse, M. Kuznetsova, Z. W. Ma, A. Bhattacharjee, A. Otto, and P. L. Pritchett, *Journal of Geophysical Research* **106**, 3715 (2001).
- [22] T. Kho and M. Haines, *Physical Review Letters* **55**, 825 (1985).
- [23] C. Ridgers, R. Kingham, and A. Thomas, *Physical Review Letters* **100** (2008), 10.1103/physrevlett.100.075003.
- [24] C. Liu, W. Fox, A. Bhattacharjee, A. G. R. Thomas, and A. S. Joglekar, *Physical Review E* **96** (2017), 10.1103/physreve.96.043203.
- [25] J. Ng, A. Hakim, A. Bhattacharjee, A. Stanier, and W. Daughton, *Physics of Plasmas* **24**, 082112 (2017).
- [26] C. Graziani, P. Tzeferacos, D. Lee, D. Q. Lamb, K. Weide, M. Fatenejad, and J. Miller, *The Astrophysical Journal* **802**, 43 (2015).
- [27] K. Germaschewski, W. Fox, S. Abbott, N. Ahmadi, K. Maynard, L. Wang, H. Ruhl, and A. Bhattacharjee, *Journal of Computational Physics* **318**, 305 (2016).
- [28] S. C. Wilks, W. L. Kruer, M. Tabak, and A. B. Langdon, *Physical Review Letters* **69**, 1383 (1992).
- [29] P. M. Nilson, L. Willingale, M. C. Kaluza, C. Kamperidis, S. Minardi, M. S. Wei, P. Fernandes, M. Nottley, S. Bandyopadhyay, M. Sherlock, R. J. Kingham, M. Tatarakis, Z. Najmudin, W. Rozmus, R. G. Evans, M. G. Haines, A. E. Dangor, and K. Krushelnick, *Physical Review Letters* **97**, 255001 (2006).
- [30] C. K. Li, F. H. Séguin, J. A. Frenje, J. R. Rygg, R. D. Petrasso, R. P. J. Town, O. L. Landen, J. P. Knauer, and V. A. Smalyuk, *Physical Review Letters* **99**, 055001 (2007).
- [31] J. Zhong, Y. Li, X. Wang, J. Wang, Q. Dong, C. Xiao, S. Wang, X. Liu, L. Zhang, L. An, F. Wang, J. Zhu, Y. Gu, X. He, G. Zhao, and J. Zhang, *Nature Physics* **6**, 984 (2010).
- [32] G. Fiksel, W. Fox, A. Bhattacharjee, D. H. Barnak, P. Y. Chang, K. Germaschewski, S. X. Hu, and P. M. Nilson, *Physical Review Letters* **113**, 105003 (2014).
- [33] M. J. Rosenberg, C. K. Li, W. Fox, A. B. Zylstra, C. Stoeckl, F. H. Séguin, J. A. Frenje, and R. D. Petrasso, *Phys. Rev. Lett.* **114**, 205004 (2015).
- [34] C. Niemann, W. Geckelman, C. G. Constantin, E. T. Everson, D. B. Schaeffer, A. S. Bondarenko, S. E. Clark, D. Winske, S. Vincena, B. Van Compernelle, and P. Pribyl, *Geophysical Research Letters* **41**, 7413 (2014).
- [35] D. B. Schaeffer, W. Fox, D. Haberberger, G. Fiksel, A. Bhattacharjee, D. H. Barnak, S. X. Hu, and K. Germaschewski, *Physical Review Letters* **119** (2017), 10.1103/physrevlett.119.025001.
- [36] W. Fox, A. Bhattacharjee, and K. Germaschewski, *Physical Review Letters* **106**, 215003 (2011).
- [37] W. Fox, A. Bhattacharjee, and K. Germaschewski, *Physics of Plasmas* **19**, 056309 (2012).
- [38] S. R. Titorica, T. Abel, and F. Fiuza, *Phys. Rev. Lett.* **116**, 095003 (2016).

- [39] J. Matteucci, W. Fox, A. Bhattacharjee, D. B. Schaeffer, C. Moissard, K. Germaschewski, G. Fiksel, and S. X. Hu, submitted, available arXiv:1710.08556 (2017).
- [40] Y. Matsumoto, T. Amano, T. N. Kato, and M. Hoshino, *Science* **347**, 974 (2015).
- [41] S. X. Hu, D. T. Michel, D. H. Edgell, D. H. Froula, R. K. Follett, V. N. Goncharov, J. F. Myatt, S. Skupsky, and B. Yaakobi, *Physics of Plasmas* **20**, 032704 (2013).
- [42] W. M. Manheimer, D. G. Colombant, and J. H. Gardner, *Physics of Fluids* **25**, 1644 (1982).
- [43] W. Fox, J. Park, W. Deng, G. Fiksel, A. Spitkovsky, and A. Bhattacharjee, *Physics of Plasmas* **24**, 092901 (2017).
- [44] L. Willingale, A. G. R. Thomas, P. M. Nilson, M. C. Kaluza, S. Bandyopadhyay, A. E. Dangor, R. G. Evans, P. Fernandes, M. G. Haines, C. Kamperidis, R. J. Kingham, S. Minardi, M. Notley, C. P. Ridgers, W. Rozmus, M. Sherlock, M. Tatarakis, M. S. Wei, Z. Najmudin, and K. Krushelnick, *Physical Review Letters* **105**, 095001 (2010).
- [45] L. Gao, P. M. Nilson, I. V. Igumenshchev, M. G. Haines, D. H. Froula, R. Betti, and D. D. Meyerhofer, *Physical Review Letters* **114** (2015), 10.1103/physrevlett.114.215003.
- [46] Y. Ren, M. Yamada, S. Gerhardt, H. Ji, R. Kulsrud, and A. Kuritsyn, *Physical Review Letters* **95**, 055003 (2005).
- [47] S. Zenitani and M. Hoshino, *The Astrophysical Journal* **562**, L63 (2014), arXiv:1402.7139.
- [48] R. P. Lin and H. S. Hudson, *Solar Physics*, **50**, 153 (1976).
- [49] D. A. Uzdensky, B. Cerutti, and M. C. Begelman, *The Astrophysical Journal* **737**, L40 (2011).
- [50] D. A. Larrabee, R. V. E. Lovelace, and M. M. Romanova, *The Astrophysical Journal* **586**, 72 (2002), arXiv:astro-ph/0210045.
- [51] S. Lu, Q. Lu, C. Huang, Q. Dong, J. Zhu, Z. Sheng, S. Wang, and J. Zhang, *New Journal of Physics* **16**, 083021 (2014).
- [52] S. Lu, Q. Lu, F. Guo, Z. Sheng, H. Wang, and S. Wang, *New Journal of Physics* **18**, 013051 (2016).
- [53] K. M. Schoeffler, N. F. Loureiro, R. A. Fonseca, and L. O. Silva, *Phys. Rev. Lett.* **112**, 175001 (2014).
- [54] L. Lancia, B. Albertazzi, C. Boniface, A. Grisollet, R. Riquier, F. Chaland, K. C. Le Thanh, P. Mellor, P. Antici, S. Buffechoux, S. N. Chen, D. Doria, M. Nakatsutsumi, C. Peth, M. Swantusch, M. Star-dubtsev, L. Palumbo, M. Borghesi, O. Willi, H. Pépin, and J. Fuchs, *Physical Review Letters* **113** (2014), 10.1103/physrevlett.113.235001.
- [55] Q. L. Dong, S. J. Wang, Q. M. Lu, C. Huang, D. W. Yuan, X. Liu, X. X. Lin, Y. T. Li, H. G. Wei, J. Y. Zhong, J. R. Shi, S. E. Jiang, Y. K. Ding, B. B. Jiang, K. Du, X. T. He, M. Y. Yu, C. S. Liu, S. Wang, Y. J. Tang, J. Q. Zhu, G. Zhao, Z. M. Sheng, and J. Zhang, *Physical Review Letters* **108**, 215001 (2012).
- [56] E. J. Smith, L. Davis, D. E. Jones, P. J. Coleman, D. S. Colburn, P. Dyal, and C. P. Sonett, *Science* **207**, 407 (1980).
- [57] L. F. Burlaga, N. F. Ness, M. H. Acuña, R. P. Lepping, J. E. P. Connerney, and J. D. Richardson, *Nature* **454**, 75 (2008).
- [58] A. H. Sulaiman, A. Masters, M. K. Dougherty, D. Burgess, M. Fujimoto, and G. B. Hospodarsky, *Phys. Rev. Lett.* **115**, 125001 (2015).
- [59] A. Masters, L. Stawarz, M. Fujimoto, S. J. Schwartz, N. Sergis, M. F. Thomsen, A. Retinò, H. Hasegawa, B. Zieger, G. R. Lewis, A. J. Coates, P. Canu, and M. K. Dougherty, *Nature Physics* **9**, 164 (2013).
- [60] D. Kazanas and D. C. Ellison, *Nature* **319**, 380 (1986).
- [61] A. Loeb and E. Waxman, *Nature* **405**, 156 (2000).
- [62] M. Ackermann, M. Ajello, A. Allafort, L. Baldini, J. Ballet, G. Barbiellini, M. G. Baring, D. Bastieri, K. Bechtol, R. Bellazzini, R. D. Blandford, E. D. Bloom, E. Bonamente, A. W. Borgland, E. Bottacini, T. J. Brandt, J. Bregeon, M. Brigida, P. Bruel, R. Buehler, G. Busetto, S. Buson, G. A. Caliandro, R. A. Cameron, P. A. Caraveo, J. M. Casandjian, C. Cecchi, O. Çelik, E. Charles, S. Chaty, R. C. G. Chaves, A. Chekhtman, C. C. Cheung, J. Chiang, G. Chiaro, A. N. Cillis, S. Ciprini, R. Claus, J. Cohen-Tanugi, L. R. Cominsky, J. Conrad, S. Corbel, S. Cutini, F. D'Ammando, A. de Angelis, F. de Palma, C. D. Dermer, do Couto, P. S. Drell, A. Drlica-Wagner, L. Falletti, C. Favuzzi, E. C. Ferrara, A. Franckowiak, Y. Fukazawa, S. Funk, P. Fusco, F. Gargano, S. Germani, N. Giglietto, P. Giommi, F. Giordano, M. Giroletti, T. Glanzman, G. Godfrey, I. A. Grenier, M. H. Grondin, J. E. Grove, S. Guiriec, D. Hadasch, Y. Hanabata, A. K. Harding, M. Hayashida, K. Hayashi, E. Hays, J. W. Hewitt, A. B. Hill, R. E. Hughes, M. S. Jackson, T. Jogle, G. Jóhannesson, A. S. Johnson, T. Kamae, J. Kataoka, J. Katsuta, J. Knödseder, M. Kuss, J. Lande, S. Larson, L. Latronico, M. Lemoine-Goumard, F. Longo, F. Loparco, M. N. Lovellette, P. Lubrano, G. M. Madejski, F. Massaro, M. Mayer, M. N. Mazziotta, J. E. McEnery, J. Mehault, P. F. Michelson, R. P. Mignani, W. Mitthumsiri, T. Mizuno, A. A. Moiseev, M. E. Monzani, A. Morselli, I. V. Moskalenko, S. Murgia, T. Nakamori, R. Nemmen, E. Nuss, M. Ohno, T. Ohsugi, N. Omodei, M. Orienti, E. Orlando, J. F. Ormes, D. Paneque, J. S. Perkins, M. Pesce-Rollins, F. Piron, G. Pivato, S. Rainò, R. Rando, M. Razzano, S. Razzaque, A. Reimer, O. Reimer, S. Ritz, C. Romoli, M. Sánchez-Conde, A. Schulz, C. Sgrò, P. E. Simeon, E. J. Siskind, D. A. Smith, G. Spandre, P. Spinelli, F. W. Stecker, A. W. Strong, D. J. Suson, H. Tajima, H. Takahashi, T. Takahashi, T. Tanaka, J. G. Thayer, J. B. Thayer, D. J. Thompson, S. E. Thorsett, L. Tibaldo, O. Tibolla, M. Tinivella, E. Troja, Y. Uchiyama, T. L. Usher, J. Vandenbroucke, V. Vasileiou, G. Vianello, V. Vitale, A. P. Waite, M. Werner, B. L. Winer, K. S. Wood, M. Wood, R. Yamazaki, Z. Yang, and S. Zimmer, *Science* **339**, 807 (2013), arXiv:1302.3307.
- [63] A. Balogh and R. A. Treumann, *Physics of Collisionless Shocks*, ISSI Scientific Report Series, Vol. 12 (Springer, 2013).
- [64] R. D. Blandford and J. P. Ostriker, *The Astrophysical Journal* **221**, L29 (1978).
- [65] D. Caprioli and A. Spitkovsky, *The Astrophysical Journal* **783**, 91 (2014).
- [66] K. G. McClements, M. E. Dieckmann, A. Ynnerman, S. C. Chapman, and R. O. Dendy, *Physical Review Letters* **87** (2001), 10.1103/physrevlett.87.255002.
- [67] A. Johlander, S. J. Schwartz, A. Vaivads, Yu. I. Ginzell, I. B. Peng, S. Markidis, P. A. Lindqvist, R. E. Ergun, G. T. Marklund, F. Plaschke, W. Magnes, R. J. Strangeway, C. T. Russell, H. Wei, R. B. Torbert, W. R. Paterson, D. J. Gershman, J. C. Dorelli, L. A. Avanzo, B. Lavraud, Y. Saito, B. L. Giles, C. J. Pollock, and

- J. L. Burch, *Phys. Rev. Lett.* **117**, 165101 (2016).
- [68] D. B. Schaeffer, E. T. Everson, A. S. Bondarenko, S. E. Clark, C. G. Constantin, D. Winske, W. Gekelman, and C. Niemann, *Physics of Plasmas* **22**, 113101 (2015).
- [69] D. L. Morse, W. W. Destler, and P. L. Auer, *Phys. Rev. Lett.* **28**, 13 (1972).
- [70] R. E. Lowe and D. Burgess, *Annales Geophysicae* **21**, 671 (2003).
- [71] T. Umeda, M. Yamao, and R. Yamazaki, *The Astrophysical Journal* **695**, 574 (2009).
- [72] Z. W. Yang, B. Lembège, and Q. M. Lu, *Journal of Geophysical Research: Space Physics* **117**, n/a (2012).
- [73] V. V. Lobzin, V. V. Krasnoselskikh, J. M. Bosqued, J. L. Pinçon, S. J. Schwartz, and M. Dunlop, *Geophysical Research Letters* **34** (2007), 10.1029/2006gl029095.
- [74] O. V. Gotchev, J. P. Knauer, P. Y. Chang, N. W. Jang, M. J. Shoup, D. D. Meyerhofer, and R. Betti, *Review of Scientific Instruments* **80**, 043504 (2009).